Role of interfacial adhesion on minimum wear particle size and roughness evolution

Enrico Milanese,[1] Tobias Brink,[1] Ramin Aghababaei,[2] and Jean-François Molinari[1,*]

[1]*Civil Engineering Institute, Materials Science and Engineering Institute, École Polytechnique Fédérale de Lausanne (EPFL), CH-1015 Lausanne, Switzerland*

[2]*Department of Engineering-Mechanical Engineering, Aarhus University, 8000 Aarhus C, Denmark*

(Received 24 March 2020; accepted 25 August 2020; published 7 October 2020)

Adhesion between two bodies is a key parameter in wear processes. At the macroscale, strong adhesive bonds are known to lead to high wear rates, as observed in clean metal-on-metal contact. Reducing the strength of the interfacial adhesion is then desirable, and techniques such as lubrication and surface passivation are employed to this end. Still, little is known about the influence of adhesion on the microscopic processes of wear. In particular, the effects of interfacial adhesion on the wear particle size and on the surface roughness evolution are not clear and are therefore addressed here by means of molecular dynamics simulations. We show that, at short timescales, the surface morphology and not the interfacial adhesion strength dictates the minimum size of wear particles. However, at longer timescales, adhesion alters the particle motion and thus the wear rate and the surface morphology.

DOI: 10.1103/PhysRevE.102.043001

I. INTRODUCTION

Wear, the removal of material from interacting surfaces, not only influences the durability of mechanical systems but is also a source of health concerns. Frictional processes that normally take place when a vehicle is in motion (e.g., a car's brakes being pulled together, tire on pavement) release wear particles into the air. Such airborne particles are known to be a health hazard, as they are associated with an overall increase of death risk [1,2]. In particular, the size of the airborne particles has a fundamental role in this, as particles at the nanoscale can deposit in lungs and other organs [1,3], and several countries prescribe limits to the concentration of fine particles in the air.

Wear particles can indeed be formed under different conditions—mainly because of adhesive forces, abrasion, corrosion, or surface fatigue [4]. Adhesion and abrasion, in particular, are found to be the most prevalent types of wear. The hardness contrast of the sliding bodies usually indicates which of the two types prevails in a given tribosystem. When one of the bodies is harder than the other, its asperities penetrate and scratch the soft body [4–7]. Cutting, pile-up, and ploughing are all abrasive wear mechanisms observed experimentally and numerically in different setups and at different scales [8–13]. When the sliding bodies have comparable hardness, material detachment mechanisms are mainly controlled by adhesive forces, and wear of the adhesive type prevails—we restrain ourselves to such conditions.

We thus here explore the role of adhesion on the size of wear particles, and the subsequent effects on the surface morphology, in a simplified two-dimensional setup. When adhesion is high, strong bonds develop at the interface between the two surfaces, and, during sliding, bond breaking below one of the two surfaces is favoured. Material is then removed from the solid and it is either transferred to the other surface or it comes off as a loose wear particle. Loose particles form then the third-body, which alters the system configuration and dynamics [14], before being eventually evacuated from the contact and released into the atmosphere.

Early pioneering work already put forward the concept of a critical contact size for adhesive wear particles to form upon contact [4]. More recent advances in the understanding of wear led us to a more complete picture, and we now know that different mechanisms of material transfer are observed within the adhesive wear regime. For low adhesion and light loads, wear follows an Eyring-like atom-by-atom removal mechanism [15–20]. More relevant for particle formation are higher loads and adhesion. In this regime, we now understand that the particle formation criterion [21] is defined by the competition between plastic deformation [18,21–23] and brittle fracture [21,24–27] of the contacting asperities. This transition from ductile to brittle behavior is governed by a material-dependent critical length scale d^* [21]. If the junction d formed upon contact by the colliding asperities is smaller than d^*, then the asperities deform plastically (Supplemental Material Fig. S.1(a) [28]). Vice versa, if $d \geqslant d^*$, then the asperities break, form a debris particle, and the system transitions to a three-body configuration (Supplemental Material Fig. S.1(a) [28]). The critical length scale d^* has the form

$$d^* = \Lambda \frac{w}{\tau_j^2/2G}, \tag{1}$$

where τ_j is the junction shear strength (affected by the adhesion strength and bulk properties), G is the shear modulus of the material, w is the fracture energy, and Λ is a geometrical factor (which is of order unity and takes into account the shape of the colliding asperities). This critical length scale

*jean-francois.molinari@epfl.ch

 ©2020 American Physical Society

d^* explains the resulting transition to a three-body system by a brittle mechanism, which is needed to evolve the initial surface topography into a self-affine morphology [24], and provides further insights into the process of wear debris formation [29–33]. Furthermore, consistent with the definition of Eq. (1), it has recently been shown that lower values of interfacial adhesion (i.e., lower τ_j) lead to larger debris volumes upon formation (larger d^*), if the initial surfaces are both atomistically flat except for a well-defined asperity [34].

Yet it is not clear how reductions in the interfacial adhesion strength affect the debris particle formation process for different initial surface morphologies. Frictional surfaces indeed often appear self-affine [35–38], that is they are rough over many length scales. Investigating self-affine surfaces is thus the next natural step following the understanding of the simplified case of well-defined asperities [34]. Moreover, at longer timescales the reduced interfacial adhesion also influences the motion of the debris particles, possibly altering the mechanisms that govern the roughness evolution observed in the full adhesion case [24]. Therefore, the present paper is concerned with investigations of self-affine surfaces and of the interplay between their geometry, the interfacial adhesion, and the particle formation and evolution.

II. MATERIALS AND METHODS

The study consists of two sets of molecular dynamics simulations and each set is characterized by a different simulated timescale. In both sets, dry sliding of two opposing two-dimensional (2D) surfaces is investigated, at constant temperature, normal pressure, and sliding velocity. The initial surfaces are self-affine (with Hurst exponent H between 0.3 and 1.0), and both consist of the same bulk material. Three different values of interfacial adhesion $\tilde{\gamma}$ are investigated: $\tilde{\gamma} \in \{1.0, 0.8, 0.6\}$. The interfacial adhesion is expressed in dimensionless terms as $\tilde{\gamma} = \gamma_{\text{int}}/\gamma_{\text{bulk}}$, where γ_{int} is the surface energy of passivated atoms on the surfaces and γ_{bulk} is the surface energy without any passivation. For $\tilde{\gamma} = 1.0$, the full adhesion case is recovered. For $\tilde{\gamma} < 1.0$ we speak of reduced interfacial adhesion. During the simulations, atoms belonging to a free surface are detected on the fly and the interaction potential between such atoms is re-assigned to the interfacial potential characterized by $\tilde{\gamma}$ to model passivation of the surfaces [34]. Atom interactions, both in the bulk and between the two different surfaces, are described by the same class of model pair potentials [21,24]. These potentials allow to explicitly capture at acceptable computational costs the ductile-to-brittle transition in adhesive wear that takes place in the moderate to large adhesion limit [21]. To include such transition within our simulation box, the chosen potential is characterized by d^* smaller than the horizontal box size l_x. The short-timescale set of simulations provides insights into the effects of adhesion and random surface topography upon debris particle formation, while the long-timescale simulations allow us to study the effects of adhesion on the long-term surface roughness evolution and on the wear rate.

Throughout the article, quantities are measured in reduced units, the fundamental quantities being the equilibrium bond length r_0, the bond energy ε at zero temperature, and the atom mass m.

A. Interaction potentials

All simulations belonging to this study are run with scaled versions of the same potential, which belongs to the same class of model pair potentials introduced in Ref. [21] and also used in Ref. [24]. This family of model potentials is a modified version of the Morse potential [39]:

$$\frac{V(r)}{\varepsilon} = \zeta \begin{cases} (1 - e^{-\alpha(r-r_0)})^2 - 1 & r < 1.1r_0 \\ c_1 \frac{r^3}{6} + c_2 \frac{r^2}{2} + c_3 r + c_4 & 1.1r_0 \leqslant r \leqslant r_{\text{cut}} \\ 0 & r_{\text{cut}} \leqslant r \end{cases}, \quad (2)$$

where ζ is a scaling factor that equals 1 for bulk atoms and can be smaller than 1 for surface atoms, r is the distance between two atoms, ε is the bond energy at zero temperature, r_0 is the equilibrium bond length, and $\alpha = 3.93\ r_0^{-1}$ governs the bond stiffness. The c_i coefficients are chosen such that the potential $V(r)/\varepsilon$ is continuous both in energy and force. The cut-off distance is set by r_{cut} and determines the inelastic behavior. This allows for changes in the potential tail (and, thus, in the material yield strength), while keeping the same elastic properties up to a 10% bond stretch. The potential adopted in this study to model the bulk is characterized by $r_{\text{cut}} = 1.48\ r_0$. In Refs. [21,24] this potential is called P4. The interfacial potentials, i.e., the potentials used to represent the adhesion between passivated atoms, are scaled versions of the bulk potential. Three scaling factors ζ are used, which corresponds to the three different $\tilde{\gamma}$ investigated: 1.0 (full adhesion), 0.8, and 0.6. The on-the-fly algorithm to assign surface atoms to the interfacial potential is the same adopted in Ref. [34] and works as follows. At time $t = 0$ all the atoms belong to the bulk potential. All atoms in the simulation box (except those where a thermostat or displacements are prescribed) are then checked every 1 000 time steps: if their coordination number is less or equal to n_c, they are considered to belong to a free surface and thus passivated and are re-assigned to the interfacial potential chosen for that simulation. We used $n_c = 15$ (within a radius of 2.23 r_0) as in Ref. [34].

B. Simulation geometry and boundary conditions

All simulations were performed in 2D using the molecular dynamics simulator LAMMPS [40]. We recall that two sets are investigated and that they differ for the timescale. The short timescale set is called set S, where "S" stands for "short timescale," and the long timescale set is named set L, where "L" stands for "long timescale." The simulations of set S are identified with a letter followed by two numbers (e.g., S-100-01). The letter is always "S" and stands for "short timescale," and it is followed by three digits that are representative of the value of the interfacial adhesion $\tilde{\gamma}$, and a progressive two-digit number from 01 to 45 that is linked to a set of values (H, σ, seed). Simulation S-080-01 thus indicates a short timescale simulation, with $\tilde{\gamma} = 0.8$ and $(H, \sigma, \text{seed}) = (0.5, 5\,r_0, 19)$. Details are reported in Supplemental Material Tables S.I, S.II, and S.III [28]. The simulations of set L are identified by a code made of a letter followed by a three-digit number and another letter. The first letter is always "L" for "long timescale," the following three digits represents the value of the interfacial adhesion $\tilde{\gamma}$, and the last letter identifies a set of values (H, seed, l_x). The simulation L-100-B, for

instance, indicates a long timescale simulation, with full adhesion at the interface, and $(H, \text{seed}, l_x) = (0.3, 29, 339.314\, r_0)$. Details are reported in Supplemental Material Table S.IV [28]. The main features of the two sets are summarized in Supplemental Material Tables S.I, S.II, S.III, and S.IV [28].

A simple scheme of the simulation setup is shown in Supplemental Material Fig. S.1 [28]. Two different horizontal box sizes have been adopted, i.e., $l_x = 339.314\ r_0$ (sets S and L) and $l_x = 678.627\ r_0$ (set L, see below). Periodic boundary conditions are enforced along the horizontal direction. The initial vertical box size is the same for all simulations of all sets and is $l_y = 394.823\ r_0$, the box is then allowed to expand vertically, e.g., upon debris particle formation. A constant pressure ($f_y = 0.02\ \varepsilon r_0^{-2}$) is applied on the top and bottom boundaries to press the surfaces together and avoid that the surfaces are driven away by inertia at the first collision. A constant horizontal velocity $v_{\text{ref}} = 0.01\ \sqrt{\varepsilon m^{-1}}$ is imposed on the first layer of atoms of the top surface. The bottom layer of atoms of the bottom surface is fixed. A temperature of $0.075\ \varepsilon$ (expressed in terms of equivalent kinetic energy per atom) is enforced by means of Langevin thermostats with a damping parameter of $0.05\ r_0/\sqrt{\varepsilon m^{-1}}$. On each body, the thermostats are applied to the three layers of atoms next to the layer where the fixed displacement or velocity is imposed. The time integration is performed with a time step of $0.005\ r_0/\sqrt{\varepsilon m^{-1}}$. Throughout the manuscript, the simulations duration is reported in terms of sliding distance, which can be converted in time units by dividing it by the imposed sliding velocity ($v_{\text{ref}} = 0.01\ \sqrt{\varepsilon m^{-1}}$). We can now compute the duration of the two sets: set L contains long timescale simulations, for a total of minimum 1.200 billion and maximum 3.113 billion time steps (i.e., a sliding distance of 60 000 r_0 and 155 650 r_0, respectively), while all simulations in set S are run for 40 million time steps (i.e., a sliding distance of 2 000 r_0). As the model potentials of Eq. (2) are adopted together with reduced units, physical units can be recovered when physical values are substituted for the fundamental quantities (i.e., the equilibrium bond length r_0, the bond energy ε at zero temperature, and the atom mass m). As an example, if we consider a metal ($\varepsilon \approx 0.6$ eV, $m \approx 27$ to 207 g/mol, and $r_0 \approx 1$ Å) [41], then the applied sliding speed is approximately in the range of 5 to 15 m/s, which is typical for MD simulations [10,11,33,42] and well within the capacity of experimental tests and engineering applications [4,43], and to which corresponds an integration step between 1 and 0.3 fs. Assuming the values of 1 fs for the time step and $v_{\text{ref}} = 5$ m/s, the sliding time is then 0.4 μs for the short timescale simulations, and between 12 to 31.13 μs for the long timescale set. Note that the choice of m and ε affects the sliding velocity and the sliding time, not the sliding distance, which is 2 μm for the short timescale simulations, and between 60 and 155.65 μm for the long timescale set (assuming $r_0 \approx 1$ Å).

The starting geometry of the system is obtained by filling the whole simulation box with atoms relaxed at the target temperature, and then removing a subset of them based on a purely geometric criterion to obtain two distinct rough surfaces. The self-affine morphology is generated with a random phase filter [44].

C. Self-affine surfaces

The same definitions and conventions of Ref. [24] are adopted throughout the manuscript and are briefly summarized here. For more details on fractal concepts, see Refs. [45,46].

Fractal surfaces whose heights $h(x)$ scale differently than the horizontal distance x are self-affine fractals, and they obey the scaling relation $h(\xi x) \sim \xi^H h(x)$ [45], where ξ is the scaling factor and H is the Hurst (or roughness) exponent, with $0 < H < 1$ for fractional Brownian motion (fBm) [47]. The Hurst exponent describes the correlation between two consecutive increments in the surface: if $H = 0.5$, the increments are randomly correlated (i.e., standard Brownian motion), if $0 < H < 0.5$, the increments are negatively correlated, and if $0.5 < H < 1$ the increments are positively correlated.

The generation of engineering surfaces is nonstationary and random [36], and it can be described as a nonstationary process with stationary increments. This allows to relate the fractal dimension D of the surface with its Hurst exponent H through its Euclidean dimension n [47]: $D + H = n + 1$.

For this class of surfaces, assuming a 1D surface profile, the fractal dimension D and the power law exponent α of the power spectral density are related as $\alpha = 5 - 2D$ [48,49]. Under these assumptions, a direct relation between H and α is found: $H = (\alpha - 1)/2$.

D. Surface analysis

The power spectral density (PSD) of a 1D surface $h(x)$ in terms of PSD per unit length $\Phi_h(q)$, q being the wave vector, is defined as [50]

$$\Phi_h(q) \equiv \frac{1}{L}\left|\int_L h(x) e^{-\mathrm{i}qx} dx\right|^2, \tag{3}$$

where the integral is the continuous Fourier transform of $h(x)$ and L is the surface length projected on the horizontal axis x. The surface profile $h(x)$ is a continuous function and it contains the value of the surface height at each value of the spatial coordinate x. In particular, we estimate Φ_h as

$$\Phi_h(q_n) \approx \Delta x P_h(q_n), \tag{4}$$

where $P_h(q_n)$ is the classical periodogram [50,51],

$$P_h(q_n) = \frac{1}{N}\left|\sum_{k=0}^{N-1} h_k e^{-\mathrm{i}q_n x_k}\right|^2, \tag{5}$$

the summation being the discrete Fourier transform of the surface. In fact, $h(x)$ is known only at a discrete set of N points x_k ($k = 0, 1, \ldots, N-1$), regularly sampled at an interval Δx, such that $h_k = h(k\Delta x)$ are the known values of $h(x)$. In our case, $\Delta x = L/N$, N being the number of atoms belonging to the surface of length L ($\Delta x \approx 1\ r_0$).

The Hurst exponent H can also be estimated with the height–height correlation function [45], which describes the average change of heights Δh between two points at a horizontal distance δx,

$$\Delta h(\delta x) = \langle [h(x + \delta x) - h(x)]^2 \rangle^{1/2}, \tag{6}$$

where the angle brackets indicate spatial average. H can be derived by the log–log plot of $\Delta h(\delta x)$, as the height-height correlation function scales as $\Delta h(\delta x) \sim \delta x^H$.

The surface roughness, that is the variations in height of the surface profile with respect to an arbitrary plane of reference [52], is measured here in terms of the equivalent root-mean square of heights

$$\sigma_{\mathrm{eq}} = \sqrt{\sigma_{\mathrm{top}}^2 + \sigma_{\mathrm{bottom}}^2}, \tag{7}$$

where σ_{top} and σ_{bottom} are the root-mean square of heights of the top and bottom surface, respectively. The root-mean square of heights σ of a surface profile $h(x)$ is defined as

$$\sigma = \sqrt{\frac{1}{N}\sum_{k=1}^{N} h_k^2}, \tag{8}$$

where N is the number of discretization points of the surface and h_k is the distance of the point k from the plane of reference (the surface midplane, in our case).

E. Data analysis

All the simulations were visualized with OVITO [53]. Due to the large amount of data, frames were saved every 10^6 steps for both the simulations in set L and set S.

To obtain the surface morphology and the debris particle volume, we need to define the interface between particle and surface wherever they are in contact. Assuming that the interface should have minimal length, we assign atoms to surface and particle with a simulated annealing approach [54] using a semi-grand-canonical lattice Metropolis–Monte Carlo [55] algorithm, where bonds between surface and particle atoms are penalized. The algorithm is described in detail in the Supplemental Material [28].

Data for σ and σ_{eq} is averaged over 10 consecutive data points.

The tangential force values for simulations in set S are stored every 5 000 steps and are averaged over windows of 10^6 steps to have the same discretization of the volume detection algorithm [see Fig. 2(d)].

The debris particle volume V and its initial volume V_0 are computed by multiplying the number of atoms belonging to the debris particle and the atomic volume [24,29], which is $\sqrt{3}/2\, r_0^2$.

III. RESULTS

In the following sections we discuss the results of our investigations. In Sec. III A, we find that the initial random morphology governs the initial debris particle volume, and deviations in the adhesion strength from the full adhesion regime do not have a significant influence. The minimum wear particle size in the general situation of rough surfaces is then predicted by the critical length scale of Eq. (1), with the junction shear strength given by the full adhesion case (i.e., $\tau_{\mathrm{j}} = \tau_{\mathrm{bulk}}$). At long timescales, we find that the surface morphology is self-affine with a persistent Hurst exponent, provided that the adhesion is strong enough to ensure the continuous reworking of the surfaces due to the third body

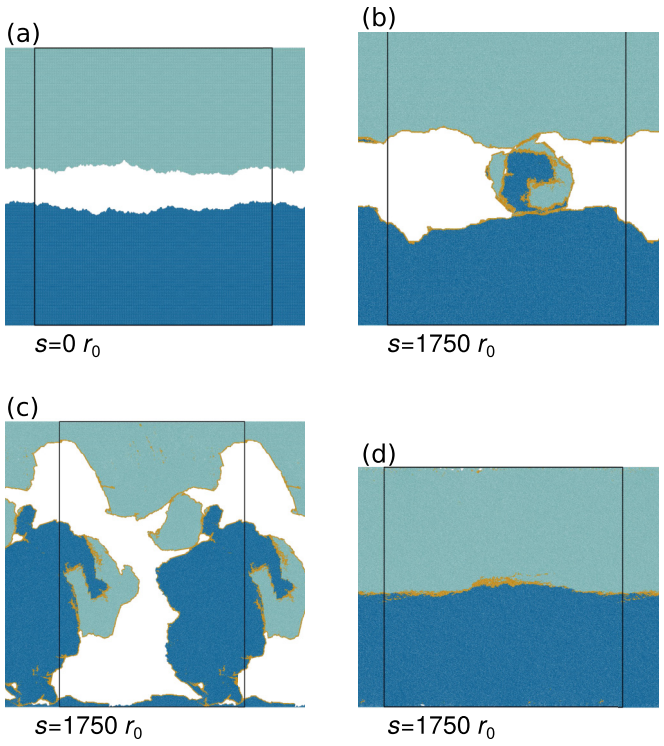

FIG. 1. Short timescale evolution. Starting from the same geometry (a), two different scenarios can develop. Either a well-defined debris particle is formed [Scenario 1, (b), full-adhesion simulation], or the effective contact spreads throughout the interface. In the latter case (Scenario 2), the system attempts to create a debris particle comparable in size with l_x [(c), simulation with $\tilde{\gamma} = 0.8$], or even larger, which results in welding of the interface within the simulated box size and damage initiating near the boundaries [(d), simulation with $\tilde{\gamma} = 0.6$]. In all panels colors distinguish atoms originally belonging to the top (light blue) and bottom (dark blue) surfaces. Atoms that at some previous instant were detected as surface atoms and reassigned to the interfacial potential are depicted in yellow. Black lines represent simulation box boundaries and s is the sliding distance in units of r_0. Frame (b) is from simulation S-100-01 (see Supplemental Material Table S.I), frame (c) is from simulation S-080-01 (see Supplemental Material Table S.II), and frame (d) is from simulation S-060-01 (see Supplemental Material Table S.III).

(Sec. III B), and that the reduced interfacial adhesion affects the wear particle growth (Sec. III C).

A. Particle formation

We first focus on the effect of surface morphology and reduced interfacial adhesion in the early stage of the adhesive wear process, when the wear debris particle is formed. We thus ran 135 short-timescale simulations (set S) with a sliding distance of 2 000 r_0. Within this set, we explored different values of the interfacial adhesion ($\tilde{\gamma} \in \{1.0, 0.8, 0.6\}$), the initial Hurst exponent ($H \in \{0.5, 0.7, 1.0\}$) and the root-mean square of heights ($\sigma \in \{5, 10, 20\}\ r_0$) of the surfaces. For each value of (H, σ), five different random seeds are used to generate five different initial fractal surfaces. The simulated timescale is large enough to fully reproduce the debris particle

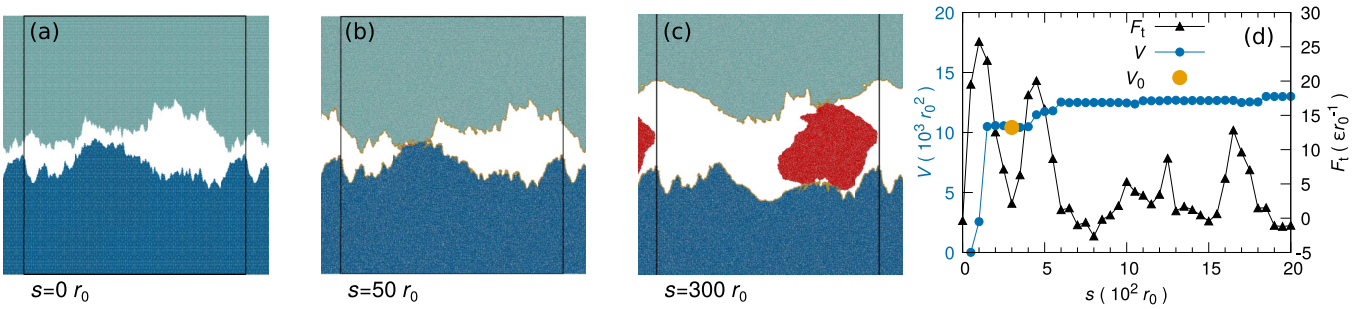

FIG. 2. Scenario 1: debris particle formation and initial volume V_0. (a–c) The surfaces, initially self-affine (a), come into contact at multiple points (b) and a peak in the tangential force F_t is recorded (d). Upon further sliding, the contact junction is large enough to generate a debris particle, whose formation is over (c) when the first local minimum of the tangential force F_t is reached (d). At this moment the initial debris particle volume V_0 is measured (d). (d) Recorded tangential force F_t (black triangles), measured debris particle volume V (blue circles) and measured initial debris particle volume V_0 (large orange circle) during a simulation that exhibits Scenario 1. In panels (a–c) colors distinguish atoms originally belonging to the top (light blue) and bottom (dark blue) bodies; in panels (b, c) colors further identify atoms that at some previous instant were detected as surface atoms and reassigned to the interfacial potential (yellow) and atoms detected as belonging to the debris particle (red); in panels (a–c) black lines represent simulation box boundaries. In all panels s is the sliding distance expressed in units of r_0. In panel (d), the volume V and the tangential force F_t are expressed in units of r_0^2 and εr_0^{-1}, respectively. Snapshots in panels (a–c) and data in panel (d) are from the reduced-adhesion simulation S-060-32 (see Supplemental Material Table S.III [28]).

formation (see Fig. 1) and obtain the initial debris particle volume V_0.

1. Conditions for particle formation

We observe that at the beginning of the sliding process, when two rough surfaces come into contact, the formation of a wear particle is complex and not well defined: Contact can develop at multiple spots along the surface, different contact junctions interact elastically [30,32], and they can coalesce into fewer, larger junctions. The process of debris particle formation is then markedly affected by the surface topography and hard to predict. This situation is more complex than the simplified case of a system with two nonrandom surfaces, e.g., two atomistically flat surfaces exhibiting each a well-defined semicircular asperity. In such case, a contact junction is clearly formed only along the contact interface of the two asperities and Eq. (1) fully describes the loose particle formation. When the two asperities come into contact, they either form a junction of size $d \geqslant d^*$ and create a wear particle immediately, or they form a junction $d < d^*$, which, upon continuous sliding, increases until $d = d^*$ and a debris particle is formed [21]. (If the asperities are not large enough, then d remains smaller than d^* and the two asperities mutually deform plastically, until the surfaces are smooth enough and welding of the interface takes place [21]).

Within the 135 simulations, two different scenarios are observed. Scenario 1: the initial collisions lead to the formation of a distinct wear debris particle [Fig. 1(b)]—this is observed in 55.6% of the cases (75 simulations). Scenario 2: multiple interacting contact junctions form or the contact spreads throughout the whole system, and a debris particle of characteristic size $d \sim l_x$ or larger would be formed. In such cases, cracks propagate from the surface until they reach the boundaries of the system [Fig. 1(c)] or the surfaces weld at the interface [Fig. 1(d)]. In the latter case, the periodic boundary conditions suppress any stress concentration required for crack propagation, and a larger system size would be needed to observe cracks that lead to debris particle formation. Because in Scenario 2 cracks either reach the boundaries of the simulation cell [Fig. 1(c)] or are inhibited [Fig. 1(d)], simulations that display such scenario are discarded from the analysis. Scenario 2 is observed in the remaining 44.4% (65 simulations).

The likelihood of one scenario or the other correlates with the root-mean square of heights σ of the initial surfaces (see Supplemental Material Table S.V [28]). This is due to the fact that, for a given value of $\tilde{\gamma}$, the rougher the surface, the more pronounced the asperities and valleys, and the system is more likely to form a junction size smaller than the system size l_x (Scenario 1). When surfaces are smooth, the probability of having multiple contact spots that interact and/or coalesce is larger, and the system is more likely to attempt to create a particle of characteristic size $d \sim l_x$ or larger (i.e., Scenario 2).

Scenario 1 is also observed more often when adhesion is larger (see Supplemental Material Table S.V [28]). A reduction in $\tilde{\gamma}$ is expected to reduce the junction shear strength τ_j and thus to increase the critical length scale d^* [see Eq. (1)]. As the system needs a larger junction size to create a debris particle, contact can develop at other places at the same time, increasing the likelihood of Scenario 2.

Note that when the surface roughness and the interfacial adhesion are minimum, i.e., $\tilde{\gamma} = 0.6$ and $\sigma = 5\ r_0$, no simulation displayed Scenario 1, consistent with the two effects that were just described.

For the subset of simulations that exhibit Scenario 1, i.e., a debris particle smaller than the system size is formed, the initial volume V_0 is investigated. For this, an unambiguous definition of V_0 is needed, and we use the tangential force F_t as a reference. When the two surfaces first come into contact, the tangential force F_t starts increasing. After a peak is reached, the force decreases, signaling debris particle formation and the onset of rolling (Fig. 2). We thus define V_0 as the volume of the debris particle measured at the first local minimum exhibited by F_t, after the initial peak, as it corresponds to

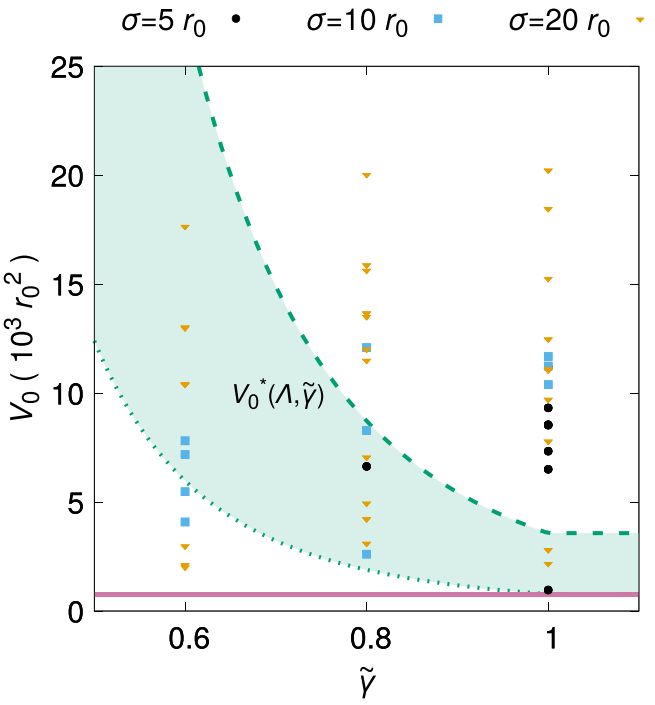

FIG. 3. Effect of interfacial adhesion $\tilde{\gamma}$ and surface morphology on the initial debris particle volume V_0. In all cases V_0 is larger than the minimum size $V_{0,\min}^*$ determined by the material critical length scale (solid purple line). The actual value $V_0 \geqslant V_{0,\min}^*$ is controlled by the random morphology. No statistically significant increase in the minimum V_0 is observed when the interfacial adhesion decreases, as would be expected by a corresponding reduction in the junction shear strength (green shaded area). The green dotted line corresponds to $V_0^*(\Lambda_{\min}, \tilde{\gamma})$ and the green dashed line to $V_0^*(\Lambda_{\max}, \tilde{\gamma})$. Each symbol identifies a unique initial surface roughness in terms of root-mean square of heights σ: $\sigma = 5\ r_0$ (black circles), $\sigma = 10\ r_0$ (light blue squares), and $\sigma = 20\ r_0$ (orange triangles). One data point ($\tilde{\gamma} = 1.0$, $V_0 = 40\,339\ r_0^2$, $\sigma = 5\ r_0$) is not represented for readability. The root-mean square of heights σ and the volume V_0 are expressed in units of r_0 and r_0^2, respectively.

the work needed to form the debris particle [29]. Identified volumes are then checked for erroneous measures, which are discarded. Erroneous measures are due to false positives of the particle detection algorithm and to the tangential force exhibiting a peak and a following local minimum when the particle is not formed yet (e.g., because of an initial ductile event). This procedure allows us to compare consistent values of V_0 from the different simulations.

The data for V_0 is reported in Fig. 3 and Supplemental Material Tables S.I, S.II, S.III, and S.V [28]. We observe (Supplemental Material Table S.V [28]) that the average value of the initial volume $\overline{V}_0$ increases with $\tilde{\gamma}$, contrary to Eq. (1). While at first this seems surprising, as lower values of $\tilde{\gamma}$ imply larger d^*, we argue that this is an artifact of the system size for low values of $\tilde{\gamma}$. When reducing $\tilde{\gamma}$, more simulations display in fact Scenario 2, i.e., the system attempts to form a debris particle that is too large with respect to the simulation cell. These cases are then not captured by the values of $\overline{V}_0$ that we measured.

When identical initial geometries are compared [i.e., for the same values of (H, σ, seed)], no correlation between the strength of adhesion and the initial volume V_0 arises. This leads to the observation that the randomness of the initial surface morphology governs the debris particle formation, in contrast to what is observed at long timescales, where the effect of adhesion is significant (see *Wear rate* paragraph).

2. Minimum particle size

We now investigate the effects of the interfacial adhesion and the morphology on the minimum size of the generated debris particle. We know that the critical length scale d^* governs the particle formation process, and that the strength of the interface enters the definition of d^* by affecting τ_j: Once a junction of size $d < d^*$ is formed, if the interface is weak the asperities slide against one another, otherwise they deform plastically [33]. We thus rewrite Eq. (1) to make explicit the effect of the interfacial adhesion,

$$d^*(\Lambda, \tilde{\gamma}) = \Lambda \frac{2Gw}{(\tilde{\gamma}\tau_{j,\text{full}})^2}, \tag{9}$$

where at the denominator the junction shear strength in the case of reduced interfacial adhesion is expressed as a reduction of the junction shear strength $\tau_{j,\text{full}}$ of the full adhesion case ($\tilde{\gamma} = 1.0$), with the proportionality given by $\tilde{\gamma}$ for the potentials adopted in this work [21]. In the limiting case of atomistically flat surfaces with semicircular asperities, this correctly predicts wear particle volumes that are larger when the interface is weaker [34]. To verify such prediction in the case of random rough surfaces, we assume that the minimum initial volume V_0^* is given by a circular particle (in two dimensions), i.e.,

$$V_0^*(\Lambda, \tilde{\gamma}) = \frac{\pi}{4} d^*(\Lambda, \tilde{\gamma})^2. \tag{10}$$

V_0^* is then minimum when Λ is minimum and $\tilde{\gamma}$ is maximum, and vice versa. In our work, the extreme values of $\tilde{\gamma}$ are the minimum and maximum input values, i.e., $\tilde{\gamma}_{\min} = 0.6$ and $\tilde{\gamma}_{\max} = 1.0$. The geometrical factor Λ is instead determined by the geometry of contact, which is hard to obtain in our case of self-affine surfaces. The two limiting cases that we assume for our simulations are flat contact ($\Lambda_{\min} = 0.70$, see Supplemental Material [28]) [32] and contact between well-defined semicircular asperities ($\Lambda_{\max} = 1.50$) [21,33]. If the reduced interfacial adhesion would play a key role in the initial debris particle volume V_0, then we would expect that

$$V_0 \geqslant V_0^*(\Lambda, \tilde{\gamma}), \tag{11}$$

where V_0 is the initial volume observed in our simulations and which is reported in Fig. 3. The green shaded area in Fig. 3 depicts the values of $V_0^*(\Lambda, \tilde{\gamma})$, where the limiting cases of $\Lambda = \Lambda_{\min}$ and $\Lambda = \Lambda_{\max}$ are given by the lower green dotted line and the upper green dashed line, respectively. Our results show that the initial debris particle volume V_0 does not obey the trend of Eq. (11), as we observe volumes V_0 measured for $\tilde{\gamma} = 0.6$ that are smaller than the expected lower bound $V_0^*(\Lambda = \Lambda_{\min}, \tilde{\gamma} = \tilde{\gamma}_{\min})$.

This shows that changes in the interfacial adhesion do not affect significantly the initial volume V_0 of the debris particle. Instead, we observe that all the recorded values of V_0 are larger than $V^*_{0,\min} = V^*_0(\Lambda_{\min}, \tilde{\gamma}_{\max})$ (solid purple line in Fig. 3), determined from the minimum d^* given in the full adhesion case ($d^*_{\text{full}} = d^*(\Lambda_{\min}, \tilde{\gamma}_{\max}) = 31.40\ r_0$, with the values of G, w, $\tau_{\text{j,full}}$ as in Ref. [21]). We ascribe such behavior to the morphology of the surfaces, which in the current work is random. Recently, a refined version of Eq. (1) was derived [33], where the junction shear strength depends on the angle of contact between the two ideal asperities. It was shown that if the angle of contact is larger than a critical value, the junction shear strength τ_{j} is given by $\tau_{\text{j,full}}$ and independent of $\tilde{\gamma}$. In the case of contact between self-affine surfaces, the contact junction is rough and the concept of angle of contact is ill-defined. Interlocking is thus expected in at least some cases. Furthermore, we argue that the ratio between the contact size and the thickness of the passivated layer also plays a significant role in the values of τ_{j}, w, and G and, thus, of V^*_0. In our simulations, the junction size is much larger than the passivated layer, which is thin when the surfaces come into contact. Since the interface has negligible volume, the fracture path leads into the bulk material and the elastic energy is also stored in the bulk material, meaning that the values of w and G are not affected by the interface strength. As argued above, the shear strength of interlocking asperities is still approximately $\tau_{\text{j,full}}$, resulting in a $V^*_0 = V^*_{0,\min}$ independent of the interface strength when asperities interlock. If the thickness of the passivated layer were large (at least larger than the contact size) and, more in general, whenever a significant component of the deformation is contained in the passivated layer, then we would expect τ_{j}, w and G to be all affected by $\tilde{\gamma}$ and d^* to differ.

We also recall that for the smoothest cases ($\sigma = 5\ r_0$), the likelihood of Scenario 1 correlates with the strength of the interfacial adhesion (Supplemental Material Table S.V [28]). In this case, the roughness is low and the deformation of the passivated layer also markedly contributes to the total deformation. This is consistent with the aforementioned argument that when the component of the deformation stored in the passivated layer is significant with respect to the total deformed volume, $\tilde{\gamma}$ affects the minimum debris particle volume [Eqs. (9) and (10)].

We thus find that for the general case of rough surfaces, and for the conditions here investigated, the surface morphology dominates the minimum size of the wear debris particles. This appears independent of reductions in the interfacial adhesion strength (within the explored range of values of reduced adhesion) and is determined by the junction shear strength in the full adhesion case (i.e., by the bulk shear strength). We do not expect the surface morphology to necessarily dominate the average size of the wear particles, where effects of interfacial adhesion are expected to emerge—larger system sizes than those used in this set of simulations are needed to explore this question.

B. Long timescale self-affine morphology

Self-affine objects differ from self-similar ones by displaying anisotropic instead of isotropic scaling [45]. For a one-dimensional surface, the scaling relation is expressed as $h(\xi x) \sim \xi^H h(x)$ [45,46], where $h(x)$ is a function describing the surface heights as a function of the spatial coordinate x, ξ is the scaling factor, and H is the Hurst (or roughness) exponent [46,47]. This relation shows how the heights scale differently than the horizontal distances, with H the scaling exponent. For physical surfaces, the Hurst exponent is constrained between 0 and 1. In the limit $H \to 1$ isotropic scaling and, thus, self-similarity are recovered. The interest in the self-affine description of surfaces lies in the fact that, for such objects, the statistics of the surface are known at any scale once the Hurst exponent is also known. This allows to gather meaningful insights at the scale that is most convenient to investigate.

To investigate the effects of the reduced interfacial adhesion on the long term evolution of the surface morphology, the set of simulations L was prepared. It is characterized by 14 long-timescale simulations—the shortest simulated sliding distance being 60 000 r_0 and the longest 155 650 r_0. Within this set, simulations differ in the interfacial adhesion ($\tilde{\gamma} \in \{1.0, 0.8, 0.6\}$), the initial Hurst exponent of the surfaces ($H \in \{0.3, 1.0\}$), and the random seed used to generate the initial fractal surfaces. We selected such values of H to avoid that the initial surfaces are already characterized by the same roughness observed at long timescales [24,35,56]. The length of the investigated timescales ensures that the whole running-in phase is over and a steady-state for the roughness in terms of equivalent root-mean square of heights σ_{eq} is reached, allowing to analyze the surface morphology in the steady-state [24]. The initial geometry is then forgotten by the system and the measured morphology is a consequence of the frictional process. During each simulation, four stages are observed. Initially, the surfaces come into contact, possibly at multiple locations as the surfaces are randomly rough. The contacting spots then deform plastically, until the junction size d is larger than d^* and a debris particle is formed [Figs. 4(a) and 4(c)]. The wear particle is then constrained to roll between the surfaces, if the interfacial adhesion is large enough [Fig. 4(b)]. Otherwise, if the adhesion is low, then the particle alternates between rolling and sticking to one surface [while sliding against the other one, Figs. 4(d)–4(f)]. When the particle rolls between the two surfaces, these are continuously worn as material is transferred back and forth between the particle and each surface.

To determine if the resulting surfaces are self-affine, we investigate both their power spectral density per unit length $\Phi(q)$ and their height-height correlation function $\Delta h(\delta x)$, where q and δx are, respectively, the wave vector and the horizontal distance between two given points on the surface. It is known in fact that, for self-affine 1D profiles, they scale as $\Phi(q) \sim q^{-2H-1}$ [47–49] and $\Delta h(\delta x) \sim \delta x^H$ [45], respectively (see Methods for more details).

Figure 5 and Supplemental Material Fig. S.2 [28] report the results of the surface analysis for the simulations in set L. The data are averaged over different independent surfaces extracted during the steady-state roughness (in terms of equivalent root-mean square of heights σ_{eq}) that follows the running-in phase [4,24,57]. While it is known that in the full adhesion case ($\tilde{\gamma} = 1.0$) surfaces display a self-affine morphology characterized by a persistent Hurst exponent [24], it

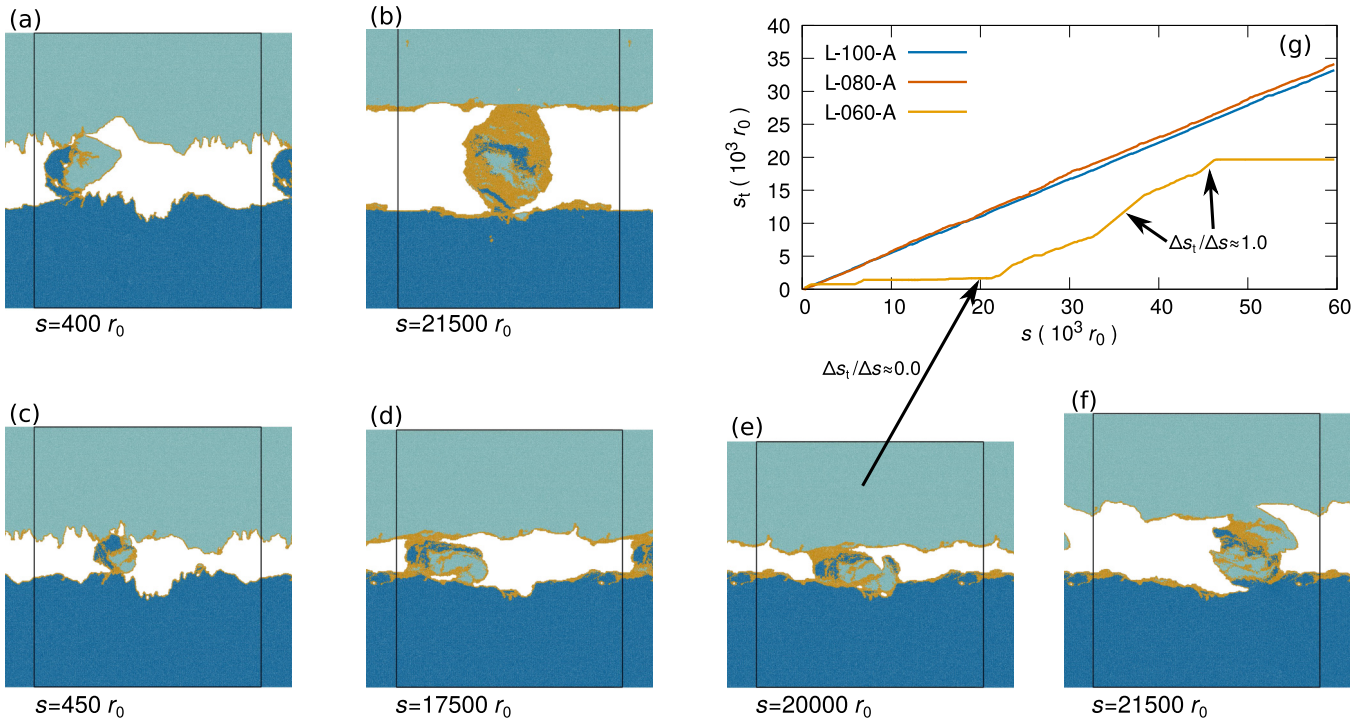

FIG. 4. Long timescale evolution and effect of adhesion on debris particle motion. (a, b) Full adhesion, $\tilde{\gamma} = 1.0$ (frames from simulation L-100-A, see Supplemental Material Table S.IV [28]). Upon sliding, contacts develop at multiple spots and grow, until cracks develop and a debris particle is formed (a). The particle then rolls between the two surfaces, wearing them and growing significantly in size (b). (c–f) Low adhesion, $\tilde{\gamma} = 0.6$ (frames from simulation L-060-A, see Supplemental Material Table S.IV [28]). Starting from the same geometry of the full-adhesion simulation of panels (a, b), upon sliding a debris particle is formed (c). This is constrained between the two surfaces and, because of the reduced interfacial adhesion and perhaps counterintuitively, it can stick for long times to one of the surfaces [e.g., the bottom one in (d)], the opposing surface sliding against the particle. The particle is gradually pushed into a valley (e) and, after a sticking time [where $\Delta s_t/\Delta s \approx 0.0$, see arrow and (g)], it detaches again with a fracture event in a two-body like configuration (f). (g) Distance s_t traveled by the debris particle as a function of the sliding distance. For full and intermediate adhesion simulations (i.e., $\tilde{\gamma} = 1.0$ and $\tilde{\gamma} = 0.8$), the particle rolls most of the time. For low adhesion cases ($\tilde{\gamma} = 0.6$), the particle undergoes long times of sticking to one surface (and sliding against the other). These periods are characterized by $\Delta s_t/\Delta s \approx 0.0$ and $\Delta s_t/\Delta s \approx 1.0$ (see arrows). In panels (a–f) colors distinguish atoms originally belonging to the top (light blue) and bottom (dark blue) surfaces. Atoms that at some previous instant were detected as surface atoms and reassigned to the interfacial potential are depicted in yellow. In panels (a–f), black lines represent the boundaries of the simulation box. Both the sliding distance s (panels a–g) and the traveled distance s_t (panel g) are expressed in units of r_0. See Supplemental Material Fig. S.3 [28] for data of s_t for further simulations.

is observed here that the self-affine description holds also in the case of reduced interfacial adhesion ($\tilde{\gamma} < 1.0$), but under some conditions.

We thus investigated the distance traveled by the debris particle in each simulation (see Fig. 4 and Supplemental Material Fig. S.3 [28]). We observe that, in simulations for which $\tilde{\gamma} = 1.0$ or $\tilde{\gamma} = 0.8$, the particle traveled a comparable distance s_t (between 30 000 and 35 000 r_0) among the different simulations, and in all cases the surfaces exhibit self-affine behavior (see Fig. 5 and Supplemental Material Fig. S.2 [28]). The traveled distance is consistent with the estimation of $s_t = s/2$ that is expected for a particle in perfect rolling conditions. To explain this expected value of $s_t = s/2$, let us assume that both the particle and the surfaces are rigid, with the top surface sliding at constant velocity v and the bottom one fixed. The highest point of the particle is then in contact with the top surface and must be sliding at velocity v. Similarly, the lowest point is in contact with the bottom surface and its velocity is zero. The center of the particle (which coincides with the center of mass) then rolls at velocity $v/2$, and the traveled distance is half the one of the top surface, within a given time period. When $\tilde{\gamma} = 0.6$, the traveled distance s_t is markedly different, the value at the end of the simulations being between 20 000 and 26 000 r_0 (see Fig. 4 and Supplemental Material Fig. S.3 [28]) or over 40 000 (see Supplemental Material Fig. S.3 [28]). These figures show that the particle undergoes long periods where it continuously slides against one of the surfaces (sticking to the other one), as significant portions at constant slope $\Delta s_t/\Delta s = 0.0$ (sticking to bottom fixed surface) and $\Delta s_t/\Delta s = 1.0$ (sticking to top sliding surface) confirm. During these periods, the particle does not roll and only works the surface against which it slides, with mechanisms that differ from the ones that take place during rolling. This is reflected by larger values of σ_{eq} (see Fig. 6) and the surfaces not always being characterized by a self-affine morphology (see Fig. 5). We believe that longer sliding distances would compensate for this effect, i.e., the overall rolling time would increase, allowing for the working

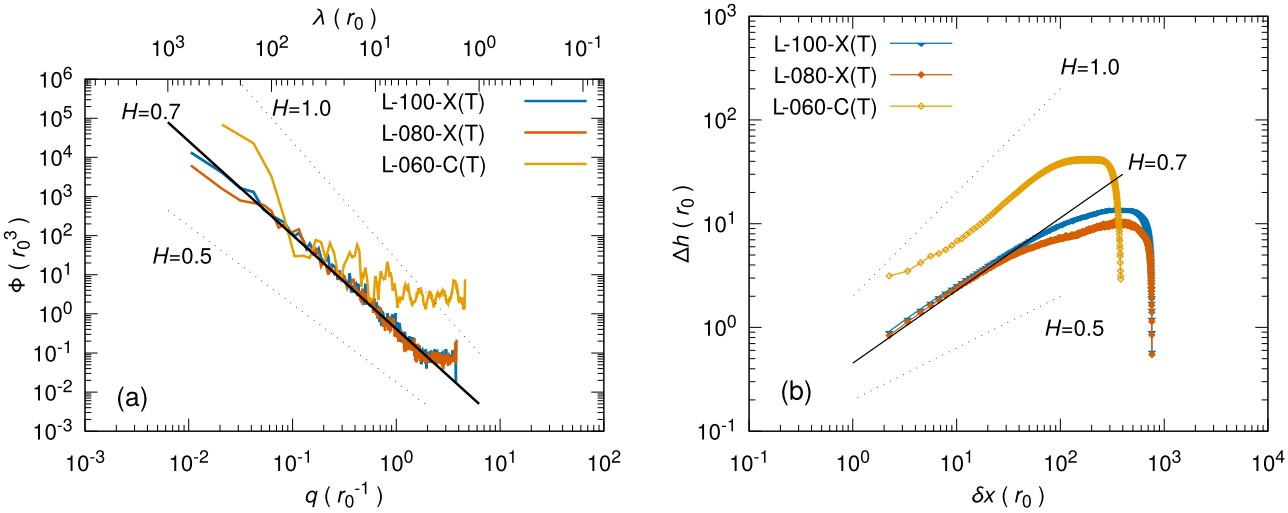

FIG. 5. Surface morphology analysis. (a) PSD per unit length Φ as a function of the wave vector q and the wavelength λ, where $q = 2\pi/\lambda$. (b) Height-height correlation function $\Delta h(\delta x) = \langle [h(x+\delta x) - h(x)]^2 \rangle^{1/2}$. The surfaces are taken from the top ("T") bodies of different simulations with different values of interfacial adhesion $\tilde{\gamma}$ and system sizes (see Supplemental Material Table S.IV for details [28]). While top surfaces of the full-adhesion simulation (L-100-X, see Supplemental Material Table S.IV [28]) and of the simulation with $\tilde{\gamma} = 0.8$ (L-080-X, see Supplemental Material Table S.IV [28]) display a self-affine morphology, this is not observed for the top surface of the simulation with $\tilde{\gamma} = 0.6$ (simulation L-060-C, see Supplemental Material Table S.IV [28]). In this case the particle traveled a longer distance s_t but did not roll for most of the simulation [see Fig. 4(b)]. In both panels the solid black straight guide-line corresponds to a Hurst exponent $H = 0.7$. Dotted black straight guide-lines show the hypothetical slope for distributions of $H = 0.5$ and $H = 1.0$. Data for all the other surfaces are reported in Supplemental Material Fig. S.2 [28]. In panel (a), the PSD per unit length Φ, the wave vector q and the wavelength λ are expressed in units of r_0^3, r_0^{-1} and r_0, respectively. In panel (b), both the height-height correlation function Δh and the horizontal distance δx are expressed in units of r_0.

of the surfaces that leads to the fractal morphology observed for larger values of the interfacial adhesion. This observation strengthens the hypothesis [24] that a frictional system needs to develop third bodies that work the surfaces for them to evolve into a self-affine topography.

C. Wear rate

The length of simulations in set L allows us to investigate also the wear rate over long distances for different values of the interfacial adhesion. Figures 6(b) and Supplemental Material Fig. S.4(b) [28] show the evolution of the wear volume

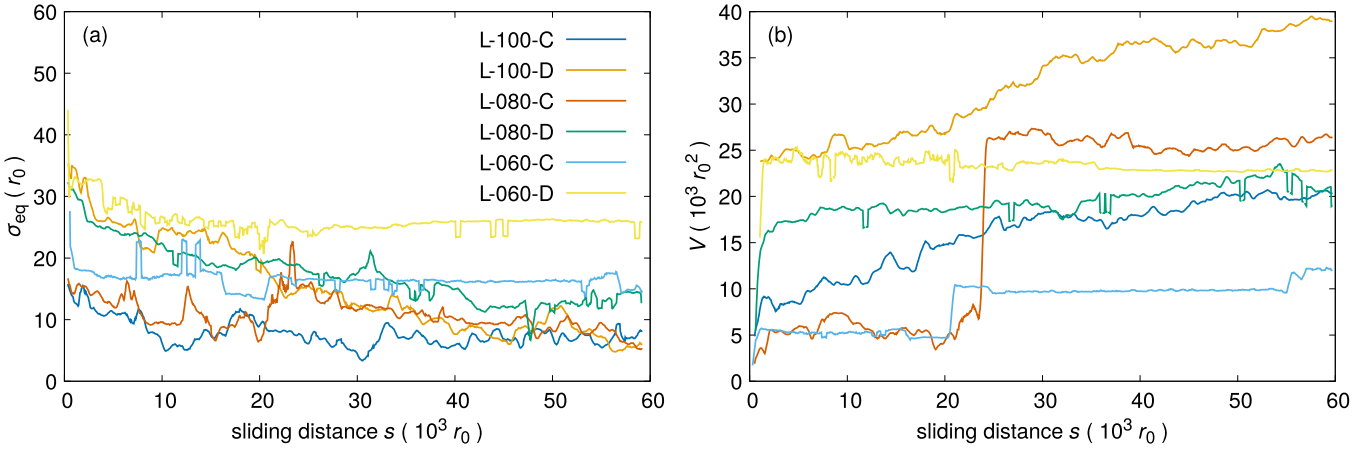

FIG. 6. Evolution of the equivalent roughness σ_{eq} and of the wear volume V. (a) Evolution of σ_{eq} for the simulations in set L (see Supplemental Material Table S.IV [28]). For simulations with $\tilde{\gamma} = 1.0$ and $\tilde{\gamma} = 0.8$, σ_{eq} decreases until a steady-state is reached, where possible fluctuations due to local events can take place. For simulations with $\tilde{\gamma} = 0.6$, the steady-state is not always reached, e.g., simulation with $\tilde{\gamma} = 0.6$ (simulation L-060-D, see Supplemental Material Table S.IV [28]), because of the long sticking times (see also Fig. 4). (b) Evolution of the wear volume V of the rolling debris particle, as defined only after its formation. The simulations with $\tilde{\gamma} = 1.0$ display steady growth of the particle volume, while simulations with $\tilde{\gamma} = 0.6$ are characterized by a negligible wear rate for most of the sliding distance, and the wear volume significantly increases only through fracturelike brittle events (see Fig. 4). Simulations with $\tilde{\gamma} = 0.8$ show an intermediate behavior. In both panels, the sliding distance s is expressed in units of r_0. The equivalent roughness σ_{eq} (panel a) and the volume V (panel b) are expressed in units of r_0 and r_0^2, respectively. Further simulations are shown in Supplemental Material Fig. S.4 [28].

V with the sliding distance s. Simulations with the lowest interfacial adhesion ($\tilde{\gamma} = 0.6$) display a markedly different behavior than the persistent increase in volume commonly expected, and observed for the full adhesion case [24]. For reduced interfacial adhesion cases, the wear volume V is characterized mostly by an almost zero wear rate, the particle volume being determined upon formation. This is due to the long sticking time. The low interfacial adhesion reduces or inhibits material transfer between the particle and the surface it slides against. And evidently no material is transferred between the particle and the surface it sticks to. Therefore the sliding motion involves only mutual deformation of the two bodies, without significant transfer of atoms (if anything, the wear particle seems to lose mass in some cases). After long periods of sticking, the deformation that takes place in the two bodies is such that the debris particle is again detached from the surface it sticks to. For example, during such a period of sticking, the particle can be pushed into a valley, then forced out of it by a fracturelike event and finally it rolls for a while, until it sticks again [Figs. 4(c)–4(f)]. These rare events can lead to significant local increases in the particle volume, as the detachment is fracture induced in a two-body configuration (Fig. 6 and Supplemental Material Fig. S.4 [28]). The growth of the debris particle volume in the low interfacial adhesion case is then not continuous and is controlled by rare fracture events.

The case for $\tilde{\gamma} = 0.8$ falls between the full and low adhesion cases. While the debris particle does not display extended sticking times, the growth rate is significantly lower than in full adhesion conditions. Rare fracture events can happen and significantly affect the wear debris volume, but they are not the predominant mechanism for mass transfer between the surfaces and the debris particle.

IV. DISCUSSION

In this study, we performed 2D molecular dynamics simulations of frictional systems to investigate the effect of reductions in the interfacial adhesion strength and initial surface morphology on three aspects of the adhesive wear process: the minimum size of loose wear particles, the long-term evolution of the surface roughness, and the wear rate. Our results show that, within the high adhesion regime that we explored, reducing the interfacial adhesion does not fundamentally change the nature of the processes occurring when two rough surfaces slide against one another and transition into a three-body configuration.

When the initial surfaces are self-affine, as is commonly expected in real applications, reducing the interfacial adhesion does not significantly affect the minimum initial volume of the debris particle that forms in the early stages of the sliding process. The random surface morphology thus governs the minimum size of the debris particles, which is then predicted by the critical length scale d^* estimated with the values of the bulk properties (full adhesion situation). This is potentially relevant to the many engineering applications where the minimum size of wear fragments is of particular interest—for instance in the transport industry, where particle emissions play an important role in health hazards that are linked to airborne particles.

Reduced interfacial adhesion nevertheless slows down some of the processes taking place during adhesive wear, namely the evolution of the surfaces into a self-affine morphology and the debris particle growth. Over long timescales, low values of interfacial adhesion increase the possibility of the debris particle to continuously slide against one of the surfaces (and stick to the other one), almost in a temporary two-body configuration, altering the wear mechanisms. If such periods are not too long with respect to the sliding distance, then the particle still has time to roll against the surfaces and work them, and the surfaces finally exhibit a self-affine morphology, otherwise no fractal scaling is observed. Furthermore, during these periods where the particle sticks to one surface, the wear rate decreases significantly and it can become negligible.

Finally, we note that these conclusions are drawn on the basis of two-dimensional simulations, as the investigated long timescales are computationally challenging for three-dimensional systems. While analogous observations have been previously extended from 2D to 3D [21,29,33], further work is needed to extend our conclusions to three-dimensional systems and to engineering applications.

ACKNOWLEDGMENTS

The calculations have been performed using the facilities of the Scientific IT and Application Support Center of EPFL. E.M. performed the numerical simulations and the analyses. R.A. developed the algorithm to detect surface atoms and reassign the interfacial potential on-the-fly. E.M., T.B., and J.-F.M. planned the simulations sets and wrote the manuscript. All authors participated in the discussion.

[1] J. M. Samet, F. Dominici, F. C. Curriero, I. Coursac, and S. L. Zeger, Fine particulate air pollution and mortality in 20 U.S. cities, 1987–1994, N. Engl. J. Med. **343**, 1742 (2000).

[2] C. A. Pope III, R. T. Burnett, M. J. Thun, E. E. Calle, D. Krewski, K. Ito, and G. D. Thurston, Lung cancer, cardiopulmonary mortality, and long-term exposure to fine particulate air pollution, JAMA **287**, 1132 (2002).

[3] U. Olofsson, A study of airborne wear particles generated from the train traffic–block braking simulation in a pin-on-disc machine, Wear **271**, 86 (2011).

[4] E. Rabinowicz, *Friction and Wear of Materials* (Wiley, New York, 1995).

[5] F. Bowden and D. Tabor, Mechanism of metallic friction, Nature **150**, 197 (1942).

[6] F. P. Bowden and D. Tabor, *The Friction and Lubrication of Solids* (Oxford University Press, Oxford, UK, 2001).

[7] K. Kato and K. Adachi, Wear mechanisms, in *Modern Tribology Handbook*, edited by B. Bhushan (CRC Press, Boca Raton, FL, 2000), Chap. 7, pp. 273–300.

[8] H. Huang, B. Lecampion, and E. Detournay, Discrete element modeling of tool-rock interaction I: Rock cutting, Int. J. Numer. Anal. Methods Geomech. **37**, 1913 (2013).

[9] S. J. Eder, D. Bianchi, U. Cihak-Bayr, A. Vernes, and G. Betz, An analysis method for atomistic abrasion simulations featuring rough surfaces and multiple abrasive particles, Comput. Phys. Commun. **185**, 2456 (2014).

[10] S. J. Eder, G. Feldbauer, D. Bianchi, U. Cihak-Bayr, G. Betz, and A. Vernes, Applicability of Macroscopic Wear and Friction Laws on the Atomic Length Scale, Phys. Rev. Lett. **115**, 025502 (2015).

[11] X. Hu and A. Martini, Atomistic simulation of the effect of roughness on nanoscale wear, Comput. Mater. Sci. **102**, 208 (2015).

[12] E. Gnecco, R. Bennewitz, and E. Meyer, Abrasive Wear on the Atomic Scale, Phys. Rev. Lett. **88**, 215501 (2002).

[13] Y. Liao and L. Marks, In situ single asperity wear at the nanometre scale, Int. Mater. Rev. **62**, 99 (2017).

[14] M. Godet, The third-body approach: A mechanical view of wear, Wear **100**, 437 (1984).

[15] H. Bhaskaran, B. Gotsmann, A. Sebastian, U. Drechsler, M. A. Lantz, M. Despont, P. Jaroenapibal, R. W. Carpick, Y. Chen, and K. Sridharan, Ultralow nanoscale wear through atom-by-atom attrition in silicon-containing diamond-like carbon, Nat. Nanotechnol. **5**, 181 (2010).

[16] A. Schirmeisen, Wear: One atom after the other, Nat. Nanotechnol. **8**, 81 (2013).

[17] T. D. Jacobs and R. W. Carpick, Nanoscale wear as a stress-assisted chemical reaction, Nat. Nanotechnol. **8**, 108 (2013).

[18] Y. Yang, L. Huang, and Y. Shi, Adhesion suppresses atomic wear in single-asperity sliding, Wear **352**, 31 (2016).

[19] Y. Shao, T. D. Jacobs, Y. Jiang, K. T. Turner, R. W. Carpick, and M. L. Falk, Multibond model of single-asperity tribochemical wear at the nanoscale, ACS Appl. Mater. Interfaces **9**, 35333 (2017).

[20] J. Liu, Y. Jiang, D. S. Grierson, K. Sridharan, Y. Shao, T. D. Jacobs, M. L. Falk, R. W. Carpick, and K. T. Turner, Tribochemical wear of diamondlike carbon-coated atomic force microscope tips, ACS Appl. Mater. Interfaces **9**, 35341 (2017).

[21] R. Aghababaei, D. H. Warner, and J.-F. Molinari, Critical length scale controls adhesive wear mechanisms, Nat. Commun. **7**, 11816 (2016).

[22] R. Holm, *Electric Contacts: Theory and Application* (Springer Science & Business Media, Berlin, 2013).

[23] A. P. Merkle and L. D. Marks, Liquid-like tribology of gold studied by *in situ* TEM, Wear **265**, 1864 (2008).

[24] E. Milanese, T. Brink, R. Aghababaei, and J.-F. Molinari, Emergence of self-affine surfaces during adhesive wear, Nat. Commun. **10**, 1116 (2019).

[25] J. Archard, Contact and rubbing of flat surfaces, J. Appl. Phys. **24**, 981 (1953).

[26] J. Liu, J. K. Notbohm, R. W. Carpick, and K. T. Turner, Method for characterizing nanoscale wear of atomic force microscope tips, ACS Nano **4**, 3763 (2010).

[27] J. Liu, D. S. Grierson, N. Moldovan, J. Notbohm, S. Li, P. Jaroenapibal, S. D. O'Connor, A. V. Sumant, N. Neelakantan, J. A. Carlisle, K. T. Turner, and R. W. Carpick, Preventing nanoscale wear of atomic force microscopy tips through the use of monolithic ultrananocrystalline diamond probes, Small **6**, 1140 (2010).

[28] See Supplemental Material at http://link.aps.org/supplemental/10.1103/PhysRevE.102.043001 for supplementary methods, figures, and tables referenced in the main text.

[29] R. Aghababaei, D. H. Warner, and J.-F. Molinari, On the debris-level origins of adhesive wear, Proc. Natl. Acad. Sci. USA **114**, 7935 (2017).

[30] R. Aghababaei, T. Brink, and J.-F. Molinari, Asperity-Level Origins of Transition from Mild to Severe Wear, Phys. Rev. Lett. **120**, 186105 (2018).

[31] L. Frérot, R. Aghababaei, and J.-F. Molinari, A mechanistic understanding of the wear coefficient: From single to multiple asperities contact, J. Mech. Phys. Solids **114**, 172 (2018).

[32] S. Pham-Ba, T. Brink, and J.-F. Molinari, Adhesive wear and interaction of tangentially loaded micro-contacts, Int. J. Solids Struct. **188**, 261 (2020).

[33] T. Brink and J.-F. Molinari, Adhesive wear mechanisms in the presence of weak interfaces: Insights from an amorphous model system, Phys. Rev. Mater. **3**, 053604 (2019).

[34] R. Aghababaei, Effect of adhesion on material removal during adhesive wear, Phys. Rev. Mater. **3**, 063604 (2019).

[35] F. Renard, T. Candela, and E. Bouchaud, Constant dimensionality of fault roughness from the scale of micro-fractures to the scale of continents, Geophys. Res. Lett. **40**, 83 (2013).

[36] R. S. Sayles and T. R. Thomas, Surface topography as a nonstationary random process, Nature **271**, 431 (1978).

[37] A. Majumdar and C. Tien, Fractal characterization and simulation of rough surfaces, Wear **136**, 313 (1990).

[38] B. Persson, O. Albohr, U. Tartaglino, A. Volokitin, and E. Tosatti, On the nature of surface roughness with application to contact mechanics, sealing, rubber friction and adhesion, J. Phys.: Condens. Matter **17**, R1 (2004).

[39] P. M. Morse, Diatomic molecules according to the wave mechanics. II. Vibrational levels, Phys. Rev. **34**, 57 (1929).

[40] S. Plimpton, Fast parallel algorithms for short-range molecular dynamics, J. Comput. Phys. **117**, 1 (1995).

[41] C. Kittel, P. McEuen, and P. McEuen, *Introduction to Solid State Physics*, Vol. 8 (Wiley, New York, 1996).

[42] X. Hu, M. V. P. Altoe, and A. Martini, Amorphization-assisted nanoscale wear during the running-in process, Wear **370**, 46 (2017).

[43] F. Bowden and D. Tabor, Friction, lubrication and wear: A survey of work during the last decade, Br. J. Appl. Phys. **17**, 1521 (1966).

[44] T. D. Jacobs, T. Junge, and L. Pastewka, Quantitative characterization of surface topography using spectral analysis, Surf. Topogr. Metrol. Prop. **5**, 013001 (2017).

[45] A.-L. Barabási and H. E. Stanley, *Fractal Concepts in Surface Growth* (Cambridge University Press, Cambridge, UK, 1995).

[46] P. Meakin, *Fractals, Scaling, and Growth Far from Equilibrium*, Vol. 5 (Cambridge University Press, Cambridge, UK, 1998).

[47] B. B. Mandelbrot, Self-affine fractals and fractal dimension, Phys. Scr. **32**, 257 (1985).

[48] S. Ganti and B. Bhushan, Generalized fractal analysis and its applications to engineering surfaces, Wear **180**, 17 (1995).

[49] M. Berry and Z. Lewis, On the Weierstrass-Mandelbrot fractal function, Proc. R. Soc. London A **370**, 459 (1980).

[50] W. H. Press, S. A. Teukolsky, W. T. Vetterling, and B. P. Flannery, *Numerical Recipes: The Art of Scientific Computing*, 3rd ed. (Cambridge University Press, Cambridge, UK, 2007).

[51] J. T. VanderPlas, Understanding the Lomb–Scargle periodogram, Astrophys. J. Suppl. Ser. **236**, 16 (2018).

[52] B. Bhushan, Surface roughness analysis and measurement techniques, in *Modern Tribology Handbook*, edited by B. Bhushan (CRC Press, Boca Raton, FL, 2000), Chap. 4, pp. 49–120.

[53] A. Stukowski, Visualization and analysis of atomistic simulation data with OVITO–The open visualization tool, Modell. Simul. Mater. Sci. Eng. **18**, 015012 (2009).

[54] S. Kirkpatrick, C. D. Gelatt, and M. P. Vecchi, Optimization by simulated annealing, Science **220**, 671 (1983).

[55] N. Metropolis, A. W. Rosenbluth, M. N. Rosenbluth, A. H. Teller, and E. Teller, Equation of state calculations by fast computing machines, J. Chem. Phys. **21**, 1087 (1953).

[56] E. E. Brodsky, J. D. Kirkpatrick, and T. Candela, Constraints from fault roughness on the scale-dependent strength of rocks, Geology **44**, 19 (2016).

[57] I. V. Kragelsky, M. N. Dobychin, and V. S. Kombalov, *Friction and Wear: Calculation Methods* (Pergamon Press, Oxford, UK, 1981).